Comparison between computer simulations and experimental data for high-rate discharges of plastic lithium-ion batteries

Pankaj Arora [a,1], Marc Doyle [b], Antoni S. Gozdz [c], Ralph E. White [a,*], John Newman [d]

[a] *Center for Electrochemical Engineering, Department of Chemical Engineering, University of South Carolina, Columbia, SC 29208, USA*
[b] *DuPont Central Research and Development, Experimental Station, Wilmington, DE 19880-0262, USA*
[c] *Telcordia Technologies (formerly Bellcore), Red Bank, NJ 07701, USA*
[d] *Department of Chemical Engineering, University of California, Berkeley, CA 94720, USA*

Abstract

Computer simulations are compared with experimental data for Bellcore PLION® cells using the graphite/1 M $LiPF_6$ in EC:DMC (2:1)/$LiMn_2O_4$ system. The motivation is to model lithium-ion polymer cells having higher active material loadings and competitive energy densities and specific energies to liquid lithium-ion batteries. Cells with different electrode thickness, initial salt concentrations, and higher active material loadings were examined using the mathematical model to understand better the transport processes in the plasticized polymer electrolyte system. A better description of the ionic conductivity is employed based on new conductivity data.

Improvements in the agreement between the simulations and experimental data are obtained by using the contact resistance at the current collector/electrode interface as an adjustable parameter for different cells, whose values vary from 20 to 35 Ω cm^2 (based on separator area). The contact resistance is believed to originate at the mesh current collector interfaces. Reducing the salt diffusion coefficient by a factor of two or more at the higher discharge rates was necessary to obtain better agreement with the experimental data. Based on the experimental data and model predictions from this study, it can be concluded that the solution-phase diffusion limitations are the major limiting factor during high-rate discharges. © 2000 Elsevier Science S.A. All rights reserved.

Keywords: Diffusion limitations; Contact resistance; Variable diffusion coefficient; Mathematical model; Plastic lithium-ion batteries; Gelled polymer electrolytes

1. Introduction

Since their introduction in 1990 by Sony, the production of lithium-ion rechargeable batteries worldwide has increased steadily, and new applications in consumer electronic devices have developed. A steady stream of advances in electrode and electrolyte materials and manufacturing technology has led to improved cell performance, especially energy density, cycle life, and low- and high-temperature performance. To bring lithium-ion batteries into high-power applications, improvements in the fundamental understanding of the rate-limiting phenomena during high-rate charge and discharge are necessary. Mathematical modeling and computer simulations represent powerful tools for gaining this fundamental understanding in a rapid and cost-effective manner.

Computer simulations have been applied to the Sony lithium-ion cell [1,2] and Bellcore PLION® lithium-ion cell [1,3]. The mathematical description is based on a macroscopic model of the full cell sandwich, which, for the Bellcore system, may consist of a lithium manganese oxide (spinel) positive electrode, a plasticized polymer electrolyte, such as 1 M $LiPF_6$ in a 2:1 mixture of EC/DMC in a copolymer matrix of polyvinylidene fluoride–hexafluoropropylene (p(VdF–HFP)), and a graphite (MCMB 2528) negative electrode [3,4]. The equations used in the mathematical model are discussed in detail elsewhere [1,2]. Direct comparisons between simulations and experimental data showed that a satisfactory description of the system was possible using macroscopic battery modeling, and several conclusions regarding battery performance and rate limitations were made. Optimization of the battery structure including electrode porosities and

---

* Corresponding author. Fax: +1-803-777-8265.

 E-mail address: white@engr.sc.edu (R.E. White).

[1] Present address: Celgard Inc., 13800 South Lakes Drive, Charlotte, NC 28210, USA.

thickness for various applications was pursued using computer-generated Ragone plots.

Adequate fitting of all the experimental data available for the Bellcore PLION® battery using the same set of parameters was possible only when additional resistance was added to the system in the form of film resistances on the electrode particles or current collectors [3]. High-rate discharges were limited primarily by transport in the solution phase of the porous electrode. Diffusion limitations in the solid insertion particles existed during discharge conditions but were minor compared to other limitations. Further work on the Bellcore system utilizing experimental and simulated impedance data implicated contact resistance on the current collector interfaces as the source of the additional high-frequency impedance in this system [5].

Improvements in cell energy density and rate capability have been made on the Bellcore PLION® system by optimizing the electrode compositions and thickness, while decreasing the volume fraction of the inactive components in the electrodes. The development of more effective surface treatments on the metal mesh current collectors has helped reduce the contact resistance while retaining high cycle life. These improvements lead to better performance but create additional challenges for battery modeling.

The description of the solution-phase transport processes in the gelled polymer electrolyte in terms of a binary electrolyte is increasingly hard to justify. It is probable that salt transport in the separator region (composed of polymer, inorganic fillers, solvents, and salt) is different from salt transport in the porous electrodes due to the different constitutions of the various regions of the cell. In particular, the volume fractions of the polymer component in the electrodes when optimized are sufficient to enable lamination of the cell layers in flexible prismatic battery designs, but are insufficient to absorb fully all the liquid electrolytic solutions present. Fundamental information about the role of the polymer component as it impacts transport processes in the porous electrodes does not yet exist. Because these processes may dominate high-rate charging and discharging of these cells, more work is needed in this important area.

The main goal of the present work is to compare computer simulations with experimental data for Bellcore PLION® cells having higher active material loadings and a range of electrode thickness. Transport limitations at high rates exist, but the agreement with experimental data becomes much poorer as the electrodes become thicker and more highly loaded. The reasons for these discrepancies are explored based on the fundamental description of salt transport in the plasticized polymer electrolyte and lithium-ion transport in the solid phase of the porous composite electrodes.

2. Description of the system

Bellcore plastic lithium-ion cells consist of porous composite positive and negative electrodes and a plasticized electrolyte, which, in the present study, was composed of 1 M $LiPF_6$ in 2:1 v/v mixture of EC/DMC, silanized fumed silica-filled p(VdF–HFP) (three parts of Kynav FLEX® 2801, two parts of silica (Cab-O-Sil® TS-530, CABOT), and five parts of dibutyl phthalate (DBP, Aldrich) by weight — pre-extraction and activation composition) copolymer matrix. The composite electrodes used in this work were a mixture of active insertion material
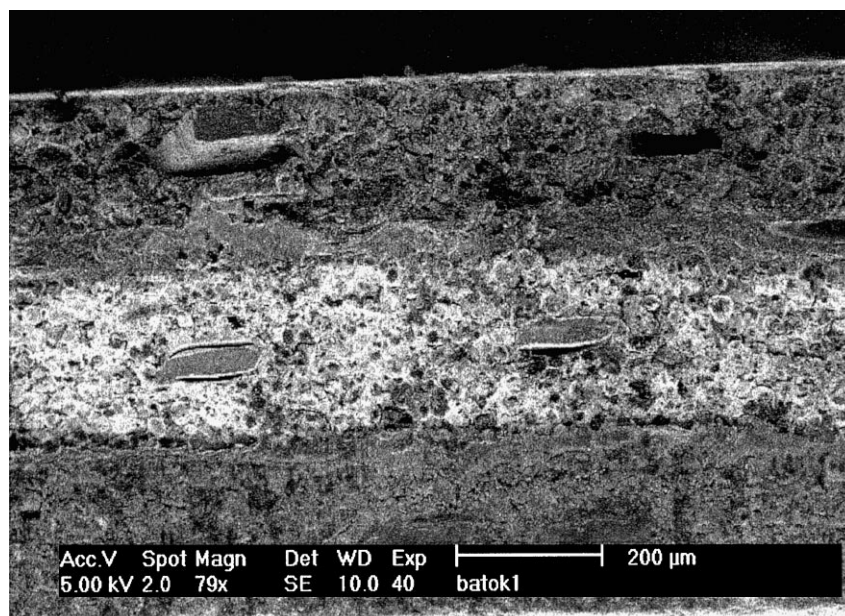

Fig. 1. SEM micrograph of PLION™ cell ($LiMn_2O_4$/graphite: bicell configuration). All active components are embedded in the chemically inert plasticized polymer matrix.

(MCMB 2528 (Osaka Gas) or $LiMn_2O_4$ (prepared in-house by Bellcore)), polymer binder, nonaqueous electrolyte, and conductive filler additive. The current collectors are expanded metal mesh made of aluminum or copper. Details of the cell fabrication process and current collector treatments have been discussed elsewhere [4,6–8].

In this study, six different cells are used to compare the model predictions with experimental data. The cells differ in their electrode thickness and initial salt concentrations. The cells with three different electrode thickness will be referred to as thin, medium, and thick cells, and the cells with different initial salt concentrations will be referred as low c^0, medium c^0, and high c^0. The thickness of the positive and negative electrode were varied from 140 to 205 μm and from 80 to 115 μm, respectively. The separator thickness was held constant at 76 μm. The cells with three different electrode thickness had an initial salt concentration of 1 M, while the cells with three different initial salt concentrations (c^0 = 0.25, 0.5, and 1.25 M) had electrode thickness of 154 (positive electrode) and 110 μm (negative electrode) and separator thickness of 100 μm.

The cells under consideration were 77.42 cm^2 (12 in.^{2}) cells with a bicell design (Al|C|S|A|Cu|A|S|C|Al). A scanning electron microscopy (SEM) cross-section of a PLION$^\circledR$ cell ($LiMn_2O_4$/graphite: bicell configuration) is

Table 1
Design-adjustable parameters

Parameter	Li_xC_6	$Li_yMn_2O_4$
Parameter		
δ (μm)		
Thin	83.5	144.4
Medium	99.0	179.3
Thick	114.7	204.4
δ_{cc} (μm)	13.6	16.0
R_s (μm)	12.5	8.5
c_s^0 (mol/dm^3)		
Thin	20.71	3.92
Medium	21.50	3.92
Thick	20.00	3.92
ε_{liq}	0.360	0.416
a (cm^{-1})^a	1226.4	1305.9
Values		
δ_s (μm)	76.2	
ε_{ls}	0.593	
ε_{ps}	0.266	
ε_{SiO_2}	0.141	
T (°C)	21.0	
c^0 (mol/dm^3)	1.00	
t_+^0	0.363	
D_0 (cm^2/s)	3.35×10^{-6}	
p		
Electrodes	5.2	
Separator	2.4	
ρ_{liq} (g/cm^3)	1.320	
ρ_p (g/cm^3)	1.750	
ρ_f (g/cm^3)	2.2	

$^a a = 3(1 - \varepsilon_{liq} - \varepsilon_p - \varepsilon_f)/R_s$.

Table 2
Parameters for the electrodes

Parameter	Li_xC_6	$Li_yMn_2O_4$
D_s (cm^2/s)	2.0×10^{-10}	1.0×10^{-9}
σ_0 (S/cm)	1.0	0.038
i_o (mA/cm^2)	0.688	0.416
c_t (mol/dm^3)	30.54	22.86
ρ (g/cm^3)	2.20	4.14

shown in Fig. 1. These have one Cu current collector in the center and two Al current collectors at the outside with two layers of anode, cathode, and separator sandwiched between the outer pair of Al current collectors. The design-adjustable parameters which include film thickness, volume fractions, particle sizes, salt concentrations, cell temperature, etc., for the first three cells (thin, medium and thick) are given in Table 1. The specific surface area per unit volume of each electrode was estimated by assuming that the electrode particles are spherical and uniform in size.

The open-circuit potentials for MCMB 2528 and $LiMn_2O_4$ electrodes as a function of state of charge have been measured previously by Doyle et al. [3] and are used as such. Few kinetic data are available for the insertion reactions, which are often characterized by reasonably high exchange current densities. The values used in this work are the same as those used previously [3]. The density of each material and exchange current density of both electrodes are given in Tables 1 and 2.

3. Polymer vs. liquid lithium-ion systems

For plastic lithium-ion batteries to compete with liquid lithium-ion cells, the excellent energy density of the latter commercial cells must be met or exceeded by the new polymer-type cells. This is an extremely challenging feat because energy densities for liquid lithium-ion cells have improved continuously since their introduction and now exceed 130 W h/kg and 300 W h/l in some medium-sized prismatic cells. For polymer-type cells to compete, the active material loadings in the electrodes must be maximized, and thickness of the electrodes must be increased to levels that are greater than are possible with liquid cells. These changes, along with the lightweight packaging, allow polymer cells to compete on an energy basis even with the thicker separators and lower active material loadings that are used in these cells. In fact, the major advantage from an energy standpoint of the polymer-type cells is their lightweight packaging, which brings significant improvements in specific energy although only modest improvements in energy density when compared to prismatic liquid lithium-ion cells on a per-cell basis.

For plastic lithium-ion battery systems, increases in active material loading have important consequences for

modeling efforts. Until now, the models in the literature for gelled polymer lithium batteries have treated the polymer electrolyte as a homogenous single-phase system. However, as polymer content in the porous electrodes is decreased, the single-phase gelled polymer electrolyte model becomes less realistic. Instead, a two-phase system probably exists, consisting of partially swollen polymer electrolyte in contact with electrode particles and relatively less free liquid electrolyte within the pores. We expect the mathematical model to be less successful in predicting the charge–discharge behavior of these current systems because of the two-phase nature of the polymer electrolyte when the cell is driven at high rates.

4. Transport properties

Knowledge of solution-phase transport property data is essential for mathematical modeling of any electrochemical system. This becomes especially important for the extended charge and discharge of lithium-ion cells because of large concentration gradients that can develop in the cell. Using constant values for the electrolyte conductivity and salt diffusion coefficient in the solution phase is not realistic as these parameters vary strongly with salt concentration. For plasticized polymer electrolyte-based cells, conductivity data on the liquid electrolytic solution as a function of salt concentration are not sufficient for a proper description of the ionic conductivity because the presence of the p(VdF–HFP) polymer and filler (silica in separator and carbon black in electrodes) affects the transport processes in the separator and porous electrodes [3]. While the literature is starting to contain more detailed transport property data on gelled polymer electrolyte systems, we are still far from having complete datasets on systems of industrial relevance [9,10].

The salt transport in the separator region of these lithium-ion polymer cells will probably be different from the salt transport in the porous electrodes because of the different constituents present in the two and because of the different pore morphologies of the films. For the system studied here, the separator region consists of EC/DMC/LiPF$_6$ and p(VdF–HFP) mixed with silanized fumed silica as the porous matrix. The electrodes, on the other hand, are composed of primarily active material and a small quantity of carbon black held together with p(VdF–HFP) and swollen with EC/DMC/LiPF$_6$. Thus, to have a good description of ionic conductivity, corrections to the conductivity expression for the neat electrolyte solution EC/DMC/LiPF$_6$ should be made for each region to account for the polymer and other components present in the system.

We have measured and incorporated a new conductivity expression as a function of salt concentration into the mathematical model. Both solution and film conductivity measurements were made for 2:1 EC:DMC electrolyte

with LiPF$_6$ salt in p(VdF–HFP)-based separators. The conductivity measurements of the salt solutions were done with a VWR Scientific conductivity probe. Ionic conductivities of the polymer films were determined from omplex impedance spectra measured using an EG&G Princeton Applied Research (model 5315) two-channel preamplifier in combination with a Wavetek 50 MHz pulse/function generator (model 165). The four-electrode conductivity cell consists of two parallel Pt wires and two stainless steel blades immobilized in a Teflon® cell separated by a fixed distance. The four-electrode configuration effectively eliminates the interfacial impedance's from the measurement of conductivity. Separator films composed of Kynar FLEX® 2801 (Elf-Atochem America), silanized fumed silica (Cab-O-Sil®, TS530), and dibutyl phthalate (DBP) (Aldrich) in a 3:2:4 mass ratio were obtained from Bellcore. The DBP was extracted from the separator using anhydrous diethyl ether (EM Industries) for 1 h followed by drying under vacuum at 60°C for 1 h before immersing the polymer films into the electrolyte. All the measurements were done inside a nitrogen-purged glove box.

The conductivity of a 2:1 v/v mixture of EC/DMC at 21°C was fit to the following function of salt concentration:

$$\kappa_{\text{liq}} = 2.905 \times 10^{-4} + 2.32702 \times 10^{-2}c - 1.82683$$
$$\times 10^{-2}c^2 + 5.1708 \times 10^{-3}c^3 - 4.977 \times 10^{-4}c^4$$
$$(1)$$

where κ_{liq} is the solution conductivity in millisiemens per centimeter and c is the salt concentration in molar. The above expression is valid over a wide range of salt concentration (0–4 M) as shown in Fig. 2. This range is sufficient, as the maximum concentration observed in these cells (from simulated concentration profiles) at very high rates is about 3.8 M.

Fig. 2 also shows the average conductivity of p(VdF–HFP)–SiO$_2$ composite films swollen in 2:1 EC/DMC as a function of salt (LiPF$_6$) concentration. The conductivity increases with salt concentration, reaches a maximum, and then decreases just as with the liquid electrolytic solutions.
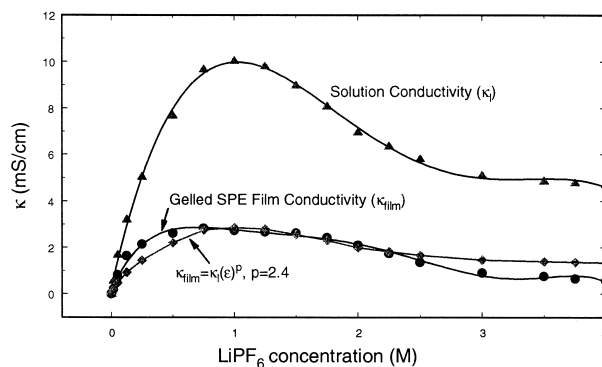

Fig. 2. Relationship between solution and film conductivity for LiPF$_6$ in a mixture of 2:1 EC/DMC in a copolymer matrix of p(VdF–HFP).

The salt concentration varied from 0.01 to 2.25 M for the measurements. Even for the highest concentration, the salt dissolved completely in the solvent mixtures. The conductivity of the p(VdF–HFP) films reaches a maximum of 3.0 mS/cm for the 1.0 M salt concentration ($\varepsilon_1 = 0.593$). The conductivity of a 2:1 v/v mixture of EC/DMC–p(VdF–HFP) film at 21°C was fit to the following function of the salt concentration:

$$\kappa_{film} = 1.436 \times 10^{-4} + 1.18731 \times 10^{-2} c - 1.95424$$
$$\times 10^{-2} c + 1.55293 \times 10^{-2} c^3 - 6.4712 \times 10^{-3} c^4$$
$$+ 1.3259 \times 10^{-3} c^5 - 1.048 \times 10^{-4} c^6 \tag{2}$$

The above fit is valid over the range of 0–4.0 M and is shown in Fig. 2. The conductivity expression given in Eq. 2 is suitable for describing the separator region. A correction should be applied before using it in the electrode region to account for the reduced solution-phase volume.

The film conductivity can also be expressed in terms of the liquid conductivity:

$$\kappa_{film} = \kappa_{liq} \varepsilon^p \tag{3}$$

where ε is the volume fraction of the electrolyte, and p is the constant whose value depends on the p(VdF–HFP) and silica contents in the different regions. The p value for the separator region was obtained by comparing the liquid conductivity data to film conductivity data using Eq. 3. p was found to be 2.4 as shown in Fig. 2. The p value for the electrode regions was determined by fitting the charge–discharge data with model predictions for all three types of cells and was found to be about 5.2. The p value obtained for the electrodes is different primarily because of the different quantity of polymer present and different morphology and pore size distribution. The different p values in the two cases suggest that a higher resistance to ionic transport exists in the porous electrodes than predicted based on the separator conductivity. This resistance could have a variety of origins as discussed later.

The diffusion coefficient of salt in the solution phase is used as a parameter to fit the experimental data. The diffusion coefficient in the porous media can also be expressed by a relationship similar to Eq. 3:

$$D_{eff} = \varepsilon^{p-1} (\varepsilon D_0) \tag{4}$$

where p is kept the same as that used for the conductivity in all three regions ($p = 2.4$ in separator and 5.2 in the two porous electrodes). ε is the volume fraction of the solution phase, and its value changes depending on the region. A constant transference number (t_+^0) of 0.363 was used to fit the experimental data for all thickness and rates [3]. The transference number used in the simulations was chosen to give the best agreement with the discharge curves of thin, medium, and thick cells. While the transference number is probably dependent on salt concentration, as shown recently for lithium bis(trifluoromethanesulfonyl)imide in EC/DMC in a p(VDF–HFP) matrix [9], the concentration

dependence is rather weak and does not appear to be of major importance for describing the current data.

Additional transport properties include the electronic conductivity and solid-phase lithium diffusion coefficient for each of the electrodes as reported in Table 2. The electronic conductivity in the electrodes was corrected for porosity and tortuosity by using a Bruggeman exponent of 1.5 [1].

5. Simulation results

One of the inputs required for the mathematical model is the initial state of charge (x^0 and y^0) of each electrode. Unfortunately, lithium stoichiometry is not an easy quantity to measure experimentally because of side reactions occurring on the negative electrode during the formation period. The values of x^0 and y^0 are determined by fitting a low-rate discharge curve to model predictions. Fig. 3 shows the comparison between simulation results and experimental data at low rates ($< C/5$). As shown in Fig. 3, very good agreement is obtained between experimental data and model predictions. The initial states of charge obtained by fitting the experimental data at small rates are reported in Table 3. The value of 0.171 was obtained for y^0, while values of 0.678, 0.704, and 0.655 were obtained for x^0 for the thin, medium, and thick cells, respectively. These same initial states of charge were used in the simulations at all discharge rates for a given cell. The values of x^0 are different for each cell, possibly because of different amounts of irreversible capacity loss in the carbon negative electrode during the formation period. The cells used in this study were formed by cycling 5–10 times before collecting the data used here. This was done to ensure that no significant capacity fade is observed during the later rate tests.

For optimum performance of lithium-ion cells, the ratio of the lithium-ion capacities of the two host materials
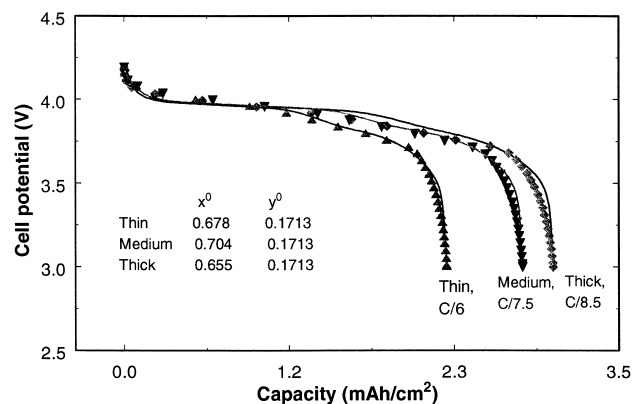

Fig. 3. Experimental and simulated discharge curves for PLION® cells at low rates. The C rates for thin, medium, and thick cells are 2.312, 2.906, and 3.229 mA/cm², respectively. The markers represent the experimental data and solid lines, the simulation results.

Table 3
Comparison of thin, medium, and thick cell data

Parameter	Thin	Medium	Thick
x^{0a}	0.678	0.704	0.655
y^{0a}	0.1713	0.1713	0.1713
C rate (mA/cm^2)	2.312	2.906	3.229
Mass ratio (γ_{actual})	2.356	2.467	2.428
Excess capacity (%)[b,c]	22.2	18.6	19.9
R_c (Ω cm^2)[a]	30.27	28.56	34.05

[a] Fitted.

[b] Based on the theoretical capacity of positive (148 mA h/g) and negative (372 mA h/g) electrodes.

[c] Excess capacity (%) = [(theoretical mass ratio − actual mass ratio)/(theoretical mass ratio)]×100%.

should be balanced. Capacity balancing refers to the optimization of the mass loading in the two electrodes to achieve the maximum capacity (or energy) from the battery under conditions of steady cycling. The condition for balanced capacities in a lithium-ion cell can be written in terms of a ratio γ of active masses in the electrodes [3]:

$$\gamma_{actual} = \frac{m_+}{m_-} = \frac{\delta_+ \varepsilon_+ \rho_+}{\delta_- \varepsilon_- \rho_-}; \quad \gamma_{theoretical} = \frac{\Delta x C_-}{\Delta y C_+} \quad (5)$$

The actual mass ratios calculated for the thin, medium, and thick cells are 2.356, 2.467, and 2.428, respectively. The theoretical mass ratio calculated on the basis of the theoretical capacity of the positive (148 mA h/g) and negative electrodes (372 mA h/g) is 3.03 when using $\Delta x = 1.0$ and $\Delta y = 0.83$. This leads to the conclusion that an excess of 22.2%, 18.6%, and 19.9% capacity exists in the negative electrode of these experimental cells. Considering also the irreversible capacity on the negative electrode (which can be 6–8% for MCMB2528 graphite), it is apparent that a wide safety margin has been designed in these cells to prevent accidental lithium deposition on the graphite during rapid charging. In packaged cells where other safety features would exist, these experimental cells could be designed differently to provide even higher energy densities by using a larger mass ratio closer to the theoretical value. The mass ratios and the percentage excess capacity for the thin, medium, and thick cells are reported in Table 3.

5.1. Solution-phase transport processes

In Fig. 4, we examine the cell potential during galvanostatic discharge of thin cells at different discharge rates ($C/6$, $C/5$, $C/2$, C, $1.5C$, $2C$, $2.5C$, and $3C$). The cell potential is plotted as a function of cell capacity (mA h/cm^2). The markers are experimental data while the solid lines represent the model predictions. The C rate for the thin cell is ca. 2.312 mA/cm^2, and the electrolyte used in all cells is the same 1 M LiPF$_6$ in 2:1 v/v mixture of EC/DMC. The simulated discharge curves without any contact resistance (not shown in Fig. 4) do not show good
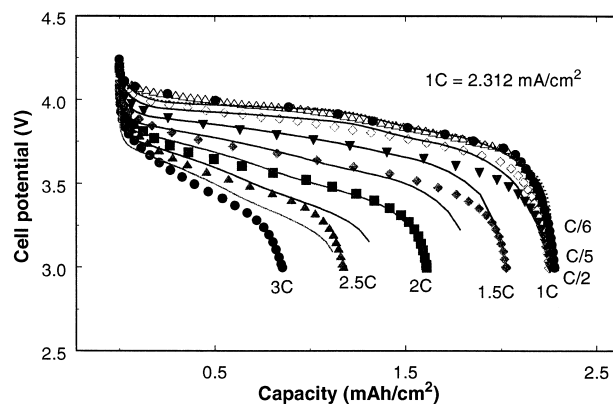
Fig. 4. Experimental and simulated discharge curves for thin cells with contact resistance ($R_c = 30.27\ \Omega$ cm^2) and constant salt diffusion coefficient. The markers represent the experimental data and solid lines, the simulation results.

agreement with the experimental data. The simulations agree well with the experimental data at low rates, but the discrepancy between model predictions and experimental data increases at higher rates as shown in Fig. 4. The diffusion limitations in the porous electrodes become more severe at higher rates, which is clear from the reduction of capacity observed at higher rates. The capacity of the thin cell at the lowest rate of 0.387 mA/cm^2 was found to be ca. 178 mA h (cell area = 77.42 cm^2). The charging rate between experimental discharge curves was 1.29 mA/cm^2, and the cutoff potentials for charging and discharging were 4.2 and 3.0 V, respectively.

Similar behavior was observed for the medium and thick cells, which are identical in design to thin cells except for the electrode thickness reported in Table 1. The agreement between model predictions and experimental data was reasonably good at low rates, but starts deteriorating at high rates. Figs. 5 and 6 show the potential of medium and thick cells as a function of capacity (mA h/cm^2) when discharged at different rates. The medium
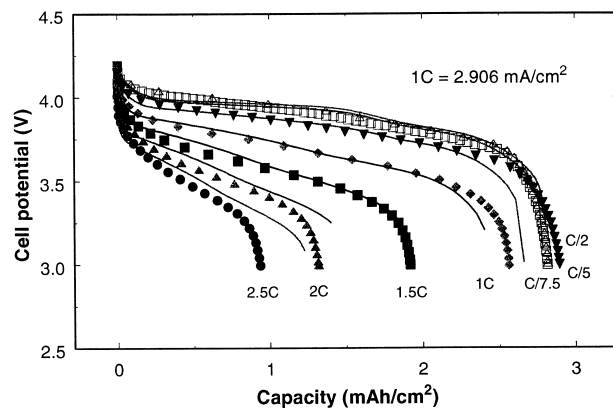
Fig. 5. Experimental and simulated discharge curves for medium cells with contact resistance ($R_c = 25.81\ \Omega$ cm^2) and constant salt diffusion coefficient. The markers represent the experimental data and solid lines, the simulation results.
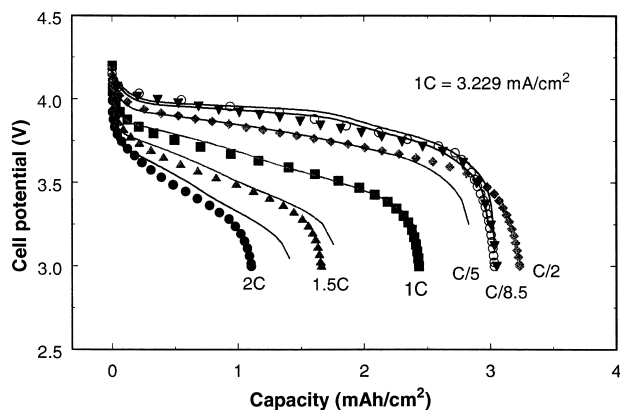
Fig. 6. Experimental and simulated discharge curves for thick cells with contact resistance ($R_c = 30.96\ \Omega\ cm^2$) and constant salt diffusion coefficient. The markers represent the experimental data and solid lines, the simulation results.

cells were discharged at the $C/7.5$, $C/5$, $C/2$, C, $1.5C$, $2C$, and $2.5C$ rates, and the thick cells were discharged at the $C/8.5$, $C/5$, $C/2$, C, $1.5C$, and $2C$ rates. The C rates for the medium and thick cells are 2.906 and 3.229 mA/cm², respectively. The capacity of the medium and thick cells at the lowest rate was ca. 224 and 248 mA h, respectively. The model simulations underpredict the experimental data at some discharge rates for all three experimental cells because capacity fade was still occurring during these cycles. The transference number and salt diffusion coefficient in the solution phase were used as adjustable parameters to fit the experimental discharge curves for the three cells. A constant transference number ($t_+^0 = 0.363$) and constant salt diffusion coefficient ($D_0 = 3.35 \times 10^{-6}\ cm^2/s$) were used to fit the experimental data at all rates simultaneously. This will be discussed in more detail in a later part of the paper.

The previous results (Figs. 3–6) have demonstrated that the agreement between the simulated discharge curves and the experimental data is unsatisfactory as the discharge rate is increased. In addition, this agreement becomes less satisfactory as the thickness of the cell is increased. Because extended high-rate discharges may be dominated by solution-phase transport processes, it is natural to consider whether our treatment of these processes needs to be modified or improved to describe best the experimental data.

Several areas can be considered for improvement, such as:

1. Inclusion of salt precipitation;
2. Allowance for solvent transport or segregation of the two solvents;
3. Allowance for convective transport;
4. Inclusion of pore wall or surface film mass transport limitations; and
5. Use of a variable salt diffusion coefficient.

Each of these areas will be considered separately to determine if they can describe the experimental findings. The calculated concentration profiles across the thin cell are shown in Fig. 7a and b for low ($0.387\ mA/cm^2$) and high ($6.936\ mA/cm^2$) rates, respectively. The concentration gradient across the cell is small during low-rate discharge as shown in Fig. 7a. During high-rate discharge, the concentration gradient across the cell is very large, and a maximum of 3.8 M salt concentration is calculated in the negative electrode as shown in Fig. 7b. The high salt concentration in the negative electrode may lead to salt precipitation, which may further lead to blocking of pores in the porous composite electrode and temporary loss of electrolyte in the cell. However, because the calculated salt concentration does not exceed 4.0 M in these cells during the highest discharge rates, which is below the solubility limit for $LiPF_6$ in 2:1 EC/DMC, the idea of including salt precipitation in the model was discarded.

As described earlier, the electrolyte (1 M $LiPF_6$ in a 2:1 mixture of EC/DMC in a p(VdF–HFP) copolymer matrix) is treated as a binary electrolyte in the present model. The
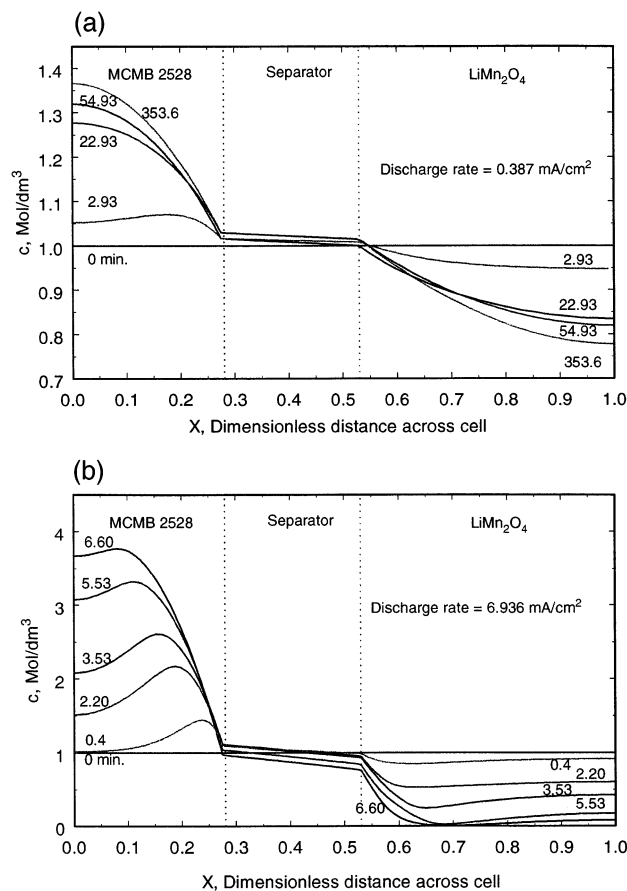

Fig. 7. (a) Simulated salt concentration profiles across the thin cell during galvanostatic discharge at the $C/6$ rate ($0.387\ mA/cm^2$). The separator region is set off by dashed lines. Times since the beginning of discharge are given in minutes. (b) Simulated salt concentration profiles across the thin cell during galvanostatic discharge at the $3C$ rate ($6.936\ mA/cm^2$). The separator region is set off by dashed lines. Times since the beginning of discharge are given in minutes.

effect of the second solvent and the polymer present in the electrolyte has not been considered directly. The different nature of the interactions between the ions and the two solvents during the passage of current may lead to segregation of the two solvents. Also, the polymer itself may not behave simply as an inert filler but may instead interact directly with the ionic species. In these cases, it is more appropriate to treat the system as a multicomponent one with the five species (polymer, EC, DMC, Li^+, and PF_6^-) leading to 10 independent transport properties. As is often the case, insufficient data exist at present for such a sophisticated treatment of the transport properties in the gelled polymer electrolyte.

In previous battery models, it has been shown that neglecting convective mass transport can be a very good approximation. Pollard and Newman [11] showed that the effect of including the convective mass transport in the Li/FeS_2 battery model was negligible. This phenomenon has not been quantified for the lithium-ion system, but we assume that the effect will be negligible here as well. The other issue of pore wall mass transport limitations has been examined previously by Doyle et al. [3] who were unable to explain high-rate transport limitations, although this topic will be revisited again at the end of this paper.

During the low-rate discharge of these cells, the change in solution-phase salt concentration across the cell is very small (see Fig. 7a) and remains close to the initial salt concentration (1 M). Hence, a constant diffusion coefficient is adequate to describe the experimental data at low rates. During high-rate discharge, a large concentration gradient is observed, as shown in Fig. 7b. The maximum concentration in the negative electrode is ca. 3.8 M, and the minimum concentration in the positive electrode is 0.0 M. A constant salt diffusion coefficient is not adequate to describe the experimental data when the change in concen-

tration across the cell is very high. Instead, a variable salt diffusion coefficient may be needed to describe the experimental data at higher rates. We attempt to fit the experimental data better by allowing the salt diffusion coefficient to vary with discharge rate for the three experimental cells (thin, medium, and thick). While this is not a physical model, it allows us to see if it is possible to describe the data by using a rate-dependent salt diffusion coefficient without having actual diffusion coefficient data as a function of salt concentration.

Until now, we have been using the porosity correction parameter p, the transference number, the salt diffusion coefficient, and the contact resistance as parameters to fit experimental data for the three different PLION® cells. The value used for the transference number is 0.363, p is 2.4 in the separator and 5.2 in the two porous electrodes, and the value of the salt diffusion coefficient (D_0) is 3.35×10^{-6} cm^2/s. The actual value of the diffusion coefficient (D_{eff}) is much smaller because of the ε^p correction applied to each region, as shown in Eq. 4. The values of contact resistance used for all three cells are given in Table 3. The source of the contact resistance based on half-cell impedance measurements on the cells is the resistance between the current collectors and electrode interfaces [5]. Next, we introduce a rate-dependent diffusion coefficient into the simulations.

Fig. 8 shows comparisons of model predictions with experimental data for thin, medium, and thick cells at moderate and high discharge rates using both contact resistance (R_c) and rate-dependent salt diffusion coefficient as parameters. The markers represent the experimental data, and solid lines represent model predictions. The simulated discharge curves show good agreement with the experimental data over the whole range. The ohmic drop in the simulations can be increased by increasing the value of
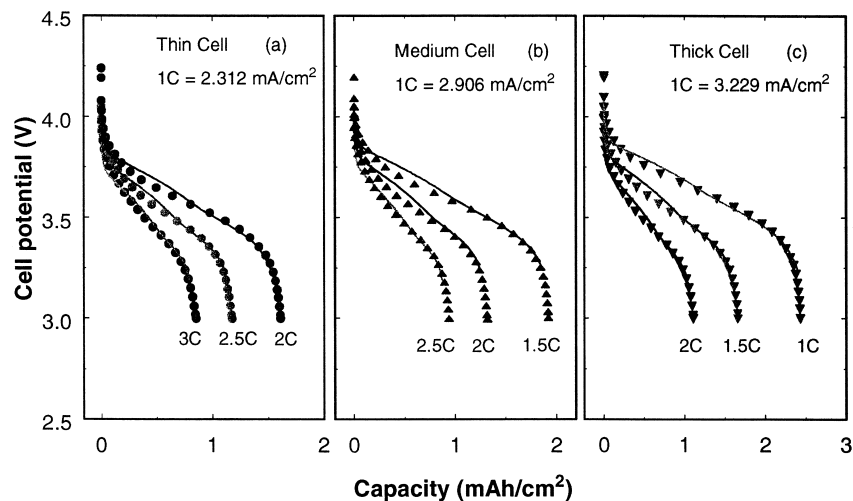

Fig. 8. Experimental and simulated moderate and high-rate discharge curves for (a) thin, (b) medium and (c) thick cells. A contact resistance (R_c = (a) 30.27, (b) 25.81 and (c) 30.96 Ω cm^2) and rate-dependent salt diffusion coefficient (see Fig. 9) were used as parameters to fit the experimental data. The markers represent the experimental data and solid lines, the simulation results.

p, but at high *p* values, the solution-phase limitations become excessive. Thus, a tradeoff between ohmic drop and solution-phase diffusion limitations is needed to describe adequately the transport processes in these lithium-ion cells. The values of contact resistance used for the thin, medium, and thick cells are 30.27, 28.56, and 34.05 Ω cm^2, respectively.

The exact value of the contact resistance (R_c) can be determined from high-frequency impedance data. The high-frequency resistance is a sum of various resistances in the cell including the contact and the bulk resistances of the electrodes and the separator. The bulk resistances of the electrodes are usually very small, and the bulk resistance of the separator is a known quantity from the separator thickness and conductivity. The remainder of the high-frequency resistance is roughly equal to the contact resistance on the current collector/electrode interfaces. Most of this contact resistance is at the aluminum current collector, but some portions of it are typically associated with the copper current collector. Half-cell impedance data can be used to determine the exact values of contact resistance on each current collector separately. In this study, the contact resistance on the two current collectors is not differentiated and is a sum of the contact resistance on the two current collectors.

The contact resistance depends critically on the type of pretreatment given to the two current collectors and it can vary from 10 to 30 Ω cm^2 for typical grid pretreatments. In this work, relatively high values of contact resistance (30.27, 28.56, and 34.05 Ω cm^2 for thin, medium and thick cells, respectively) are used to explain the experimental data in the absence of impedance data for these particular cells. The contact resistance can be modified (lowered) by incorporating the additional resistances into the other ohmic parameter, *p*, which is the effective ionic conductivity in the separator and porous electrodes. The value of *p* in separator region was determined to be 2.4 as shown in Fig. 2, but the value of *p* in the porous electrodes ($= 5.2$) was determined by comparing the model predictions with the experimental data. Thus, the value of R_c can be offset partially by increasing or decreasing the value of *p* in the porous electrodes. The type of current collector pretreatment can also explain the high value of R_c in the experimental cells used in this study.

The agreement between the solid lines and markers is good for low discharge rates but is not as good for high discharge rates even with the adjustable parameters discussed above. Considering the case of the thin cells, a constant diffusion coefficient (3.35×10^{-6} cm^2/s) was used to fit the experimental data obtained at low discharge rates (0.387–4.624 mA/cm^2, or from $C/6$ to $2C$), but at high rates ($2.5C$ and $3C$), the diffusion coefficients used were lower (2.65 and 1.85×10^{-6} cm^2/s). Thus, a smaller diffusion coefficient (D_0) is needed to obtain the best fit to discharge curves at higher rates. Similar behavior was observed for the medium and thick cells.
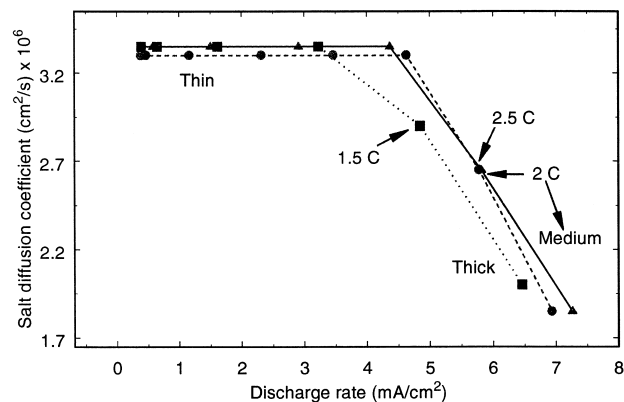

Fig. 9. Salt diffusion coefficient as a function of discharge rate for thin, medium, and thick lithium-ion cells giving the best fit to the experimental data. A lower diffusion coefficient was needed at the $2C$ rate for thin cell ($C \sim 2.312$ mA/cm^2), $1.5C$ rate for medium cell ($C \sim 2.906$ mA/cm^2), and $1.2C$ rate for thick cell ($C \sim 3.229$ mA/cm^2).

It appears that a variable diffusion coefficient (rate-dependent) should be incorporated in the model for the proper description of transport in the system. Fig. 9 gives the values of the optimized salt diffusion coefficient used to fit the experimental data at different discharge rates for all three type of cells. A constant diffusion coefficient was sufficient to fit the experimental data up to a certain C rate. At higher rates, a lowering of the salt diffusion coefficient was observed for all three cells as shown in Fig. 9. For thin cells, lower diffusion coefficients were needed for rates higher than $2.5C$, while for medium and thick cells, lower values of diffusion coefficients were needed for rates higher than $2C$ and $1.5C$, respectively. Hence, solution-phase diffusion limitations become more prominent as the thickness of the electrodes increases.

As no experimental data for salt diffusion coefficient as a function of salt concentration are available in the literature, we incorporated several different expressions in the model to see if any of these functional forms could describe the experimental data. Linear, polynomial, and exponential relationships were tried. We would normally expect D_{salt} to decrease with increasing concentration owing to ion–ion interactions at high salt concentrations [12]. Some of the expressions ($D = f(c)$) used are shown below:

Linear expressions:

$$D = D_0 + m(1 - c) \tag{6}$$

and

$$D = 3.35 \times 10^{-10} \text{ when } c < 2.5 \text{ M},$$
$$D = D_0(m - c) \text{ when } c > 2.5 \text{ M} \tag{7}$$

Exponential expression:

$$D = D_0 \exp(mc) \tag{8}$$

Polynomial expressions:

$$D = m[f(\kappa_{soln})], \qquad \text{where } \kappa_{soln} = f(c) \tag{9}$$

and,

$$D = D_0\left(a_1 + a_2 c + a_3 c^2 + a_4 c^3 + \dots\right). \qquad (10)$$

Each of the above expressions (Eqs. 6–10) for $D = D(c)$ was used in the computer simulations, but none of them could fit the whole data set well without any additional adjustable parameters. As we have tried various functional expressions for salt diffusion coefficient (Eqs. 6–10), it is unlikely that experimental data for salt diffusion coefficient as a function of salt concentration will provide satisfactory fits.

5.2. Solid-phase transport processes

High-rate discharges are limited by diffusion processes, which can exist in either the solution or solid phase or both. In Section 5.1, it was shown that diffusion limitations in the solution phase are a possible cause for rate limitations at high rates, but it is still not clear whether they are the main limitation. The solid-phase concentration profiles in the particles of both positive and negative electrodes clearly show that diffusion limitations also exist in the solid phase during discharge at high rates. In fact, it has been shown previously that a properly designed lithium-ion cell should have transport limitations in both phases during high rate use so that both energy density and power density in the cell are optimized [3].

The comparison between computer simulations and experimental data for thin, medium, and thick cells at moderate and high discharge rates is shown in Fig. 10. All the parameters used were identical to those in Section 5.1 and are shown in Tables 1 and 2. The model predictions were done with a constant salt diffusion coefficient (3.35×10^{-6} cm^2/s) in the solution phase, a constant solid-phase diffusion coefficient (2×10^{-10} cm^2/s) in the negative electrode, and various solid-phase diffusion coefficients in the positive electrode. The model predictions are in good agreement with the experimental data at all rates.
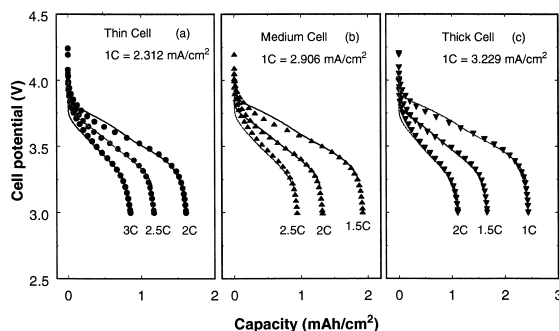

Fig. 10. Experimental and simulated moderate and high-rate discharge curves for (a) thin, (b) medium and (c) thick cells. A contact resistance (R_c = (a) 30.27, (b) 25.81 and (c) 30.96 Ω cm^2) and rate-dependent solid-phase diffusion coefficient (see Fig. 11) in the positive electrode were used as parameters to fit the experimental data. The value of salt diffusion coefficient used was 3.35×10^{-6} cm^2/s. The markers represent the experimental data and solid lines, the simulation results.
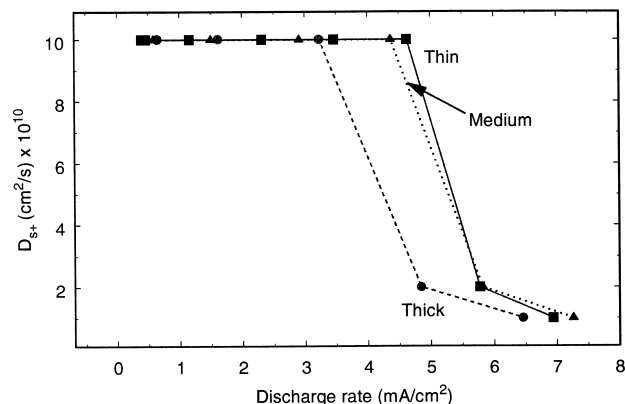

Fig. 11. Solid-phase diffusion coefficient in the positive electrode as a function of discharge rate for thin, medium, and thick lithium-ion cells giving the best fit to experimental data.

At low rates, a constant solid-phase diffusion coefficient ($D_{s+} = 1 \times 10^{-9}$ cm^2/s) was sufficient to describe the experimental data, but at higher rates, lower diffusion coefficients ($D_{s+} \leq 2 \times 10^{-10}$ cm^2/s) were needed. At low rates, the effect of changing the diffusion coefficient is minor, and good fits can be obtained when $D_{s+} \geq 3$–4×10^{-10} cm^2/s, but at higher rates, a small change in the diffusion coefficient leads to significant changes in the discharge profiles. This is because at high-rate discharges, the cell performance is reduced by the diffusion limitations in the solid phase. Similar behavior was observed for all three types of cells. Fig. 11 shows the values of solid diffusion coefficient in the positive electrode used to obtain the best fit to the experimental data. The solid-phase diffusion coefficients in the negative electrode were also varied to see whether experimental data could be described better with a composition-dependent diffusion coefficient. The fits obtained by varying D_{s-} were not as good as those obtained by varying either D_{s+} or the salt diffusion coefficient, especially for the medium and thick cells.

5.3. Initial salt concentration

The comparison of model predictions with experimental data has demonstrated that diffusion limitations existing in either the solution or solid phase of the composite positive electrode can be used to fit the data adequately. It is not yet clear which is the major limitation during high-rate discharge. One might expect cells with higher or lower initial bulk salt concentrations to have a different degree of solution-phase diffusion limitations. In particular, lower initial salt concentrations should promote a greater degree of diffusion limitations in the solution phase. On the other hand, modifications to the electrode active material particle size would be expected to impact on solid-phase transport limitations while not having a significant influence on solution-phase diffusion processes. We decided to attempt the former approach and modify the initial salt concentration in experimental cells in order to impact solution-phase

diffusion limitations. We reason that this should have a major effect on the cell's rate capability if solution-phase diffusion limitations are the primary cause of rate limitations in the experimental cells.

Cells with three different initial salt concentrations (c^0 = 0.25, 0.5, and 1.25 M) were used to determine the major limiting factor during high-rate discharges. All other design and system parameters were the same as shown in Tables 1 and 2. Figs. 12–14 show comparisons of model predictions with experimental data for cells with three different salt concentrations at various discharge rates ($4C$, $3C$, $2C$, $1C$, $C/2$, $C/5$, and $C/10$, $1C \sim 2.312$ mA/cm^2) using both contact resistance (R_c = 20.31, 23.63, and 19.16 for cells with c^0 = 0.25, 0.5, and 1.25 M, respectively) and salt diffusion coefficient as parameters. The markers represent the experimental data, and solid lines represent model predictions. The simulated discharge curves show good agreement with the experimental data over the whole range of discharge rates. A lower salt diffusion coefficient was again needed at high rates to describe the experimental data. The simulations were also carried out with a rate-dependent solid-phase diffusion coefficient for the positive electrode. It was found that very good agreement could be obtained for the cell with high initial salt concentration (c^0 = 1.25 M), but the agreement was not good for cells with low initial salt concentration (0.25 and 0.5 M), especially during high-rate discharges. It can be concluded that solution-phase diffusion limitations are the major limiting factor during high-rate discharges.

Fig. 15 compares the experimental and predicted discharge capacities for cells with three different initial salt concentrations. The solid symbols represent the experimental discharge capacity, while the open symbols represent the simulated discharge capacity. The model predictions match reasonably well with the experimental data when a rate-dependent salt diffusion coefficient is used. The inflection at high rates is due to the time required to develop
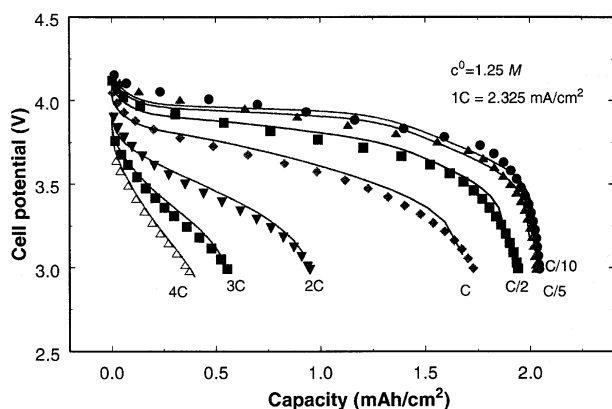

Fig. 13. Experimental and simulated discharge curves for a cell with low initial salt concentration (c^0 = 0.5 M). A contact resistance (23.63 Ω cm^2) and rate-dependent salt diffusion coefficient (see Fig. 16) were used to fit the experimental data. The markers represent the experimental data and solid lines, the simulation results.
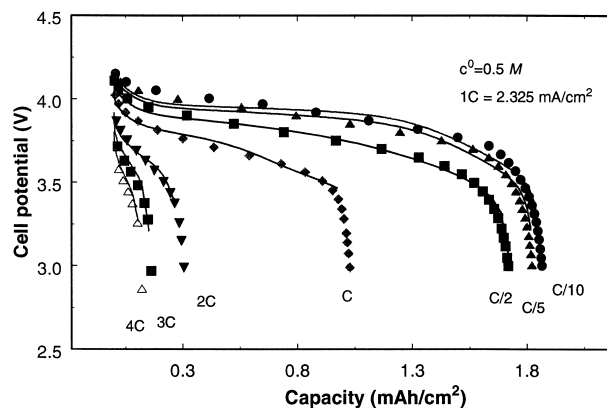
the salt concentration gradients inside the cell. Fig. 16 shows salt diffusion coefficients used to fit the experimental data at different discharge rates for the three cells with different initial salt concentrations. At low rates, a constant salt diffusion coefficient was again sufficient to describe the experimental data, but at high rates, different values were needed. The values used for the three cells at low rates probably reflect the true concentration dependence of the salt diffusion coefficient. At high rates, the solution-phase diffusion limitations start to dominate, and a lower salt diffusion coefficient is needed to describe the experimental data. The solution-phase diffusion limitations are more severe for cells with the lowest initial salt concentration (c^0 = 0.25 M) as reflected in the magnitude of the decrease in D_{salt} needed to describe the data.

After examining the experimental data and model predictions for cells with three different initial salt concentrations, the exact reason for the discrepancies between the
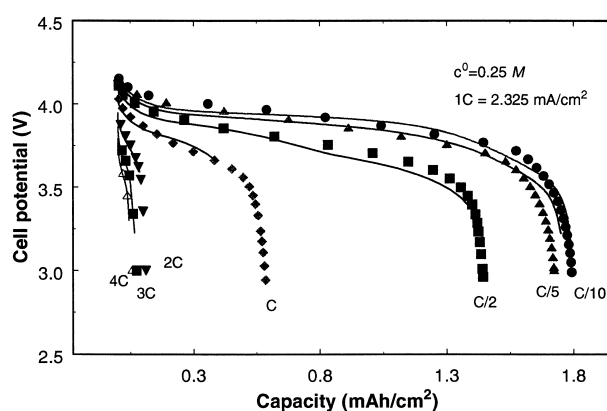

Fig. 12. Experimental and simulated discharge curves for a cell with high initial salt concentration (c^0 = 1.25 M). A contact resistance (19.16 Ω cm^2) and rate-dependent salt diffusion coefficient (see Fig. 16) were used to fit the experimental data. The markers represent the experimental data and solid lines, the simulation results.

Fig. 14. Experimental and simulated discharge curves for a cell with low initial salt concentration (c^0 = 0.25 M). A contact resistance (20.31 Ω cm^2) and rate-dependent salt diffusion coefficient (see Fig. 16) were used to fit the experimental data. The markers represent the experimental data and solid lines, the simulation results.

model and experiments is still not clear. Earlier, we suggested that the description of the transport processes in the gelled polymer electrolyte component of the battery needed to be improved. First, the different compositions in the various battery layers need a more detailed description and accounting in the modeling. For example, while the separator layer is composed of polymer, liquid electrolyte, and filler such as fumed silica, the electrodes are composed of polymer and liquid electrolyte in a different ratio as well as active materials and carbon black. It is well-known that the ratio of polymer to liquid electrolyte in gelled polymer electrolytes has a major impact on ionic transport properties.

Based on the present observations, we conclude that the transport processes in the gelled polymer electrolyte are indeed the main cause of rate limitations in these cells. However, the binary electrolyte description, which has been used to date to describe these processes, needs improvement. We suggest that the physical structure and possibly the process for making the electrode layers need to be considered in the model description. Based on the present formulations being employed, a better description of the physical situation may consist of electrode particles partially covered by gelled polymer electrolyte with interstitial spaces filled with essentially liquid electrolyte. The gelled polymer electrolyte phase covering the particles may be incompletely gelled and may have a lower conductivity than that of the separator layer, for example. This layer would present a significant diffusional and ohmic barrier during operation of the battery that cannot be described adequately using the single-phase gelled polymer electrolyte description currently in use.

The physical picture we are describing can be translated into a mathematical model by considering transport in the direction perpendicular to the pore direction (which we shall call the z-direction). This pore wall transport is
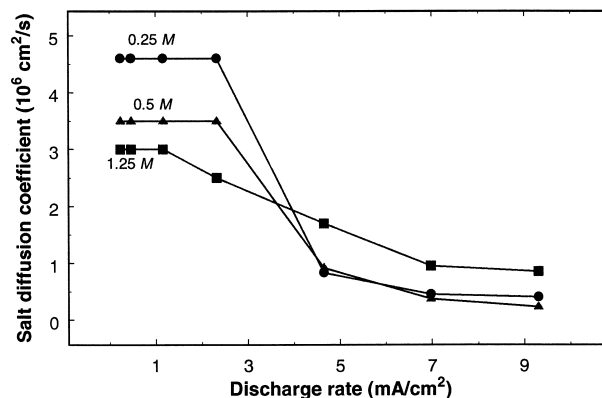
Fig. 16. Salt diffusion coefficient as a function of discharge rate for cells with three different initial salt concentrations ($c^0 = 0.25$, 0.5 and 1.25 M) giving the best fit to the experimental data.

usually ignored in favor of the x-direction in most battery models due to geometric considerations. However, if the transport properties are significantly reduced in one direction vs. the other, this assumption needs to be revisited. The simplest procedure for describing the mass transport limitations in the z-direction is to make a pseudo-steady-state assumption and utilize the mass transfer coefficient approach [3]. As this was attempted already and was not successful, we assume that a two-dimensional battery model is now required to resolve these questions. The two-dimensional model supplemented with transport property measurements will lead to a better understanding of the diffusion limitations (both solution and solid phase) in these cells.

6. Conclusion

The solution and p(VdF–HFP)-based film conductivity for $LiPF_6$ in 2:1 EC/DMC is reported as a function of salt concentration. An improved description of ionic conductivity is incorporated into a macroscopic mathematical model to describe the transport processes in the cell. The computer simulations are compared to experimental data for cells having different electrode thickness. Good agreement between theory and experiment is obtained by using the contact resistance at the electrode/current collector interface as an adjustable parameter for different cells and by using a rate-dependent salt diffusion coefficient in the solution phase. Additional resistances present in the experimental cells can be attributed to the contact resistance between the metal mesh current collectors and the composite electrodes.

At low rates, a single diffusion coefficient was sufficient to describe the experimental data, while at high rates, lower values were needed. This highlights the need for variable transport property data in the mathematical model-
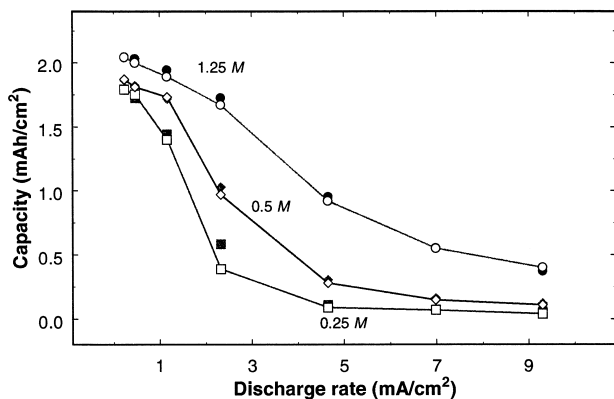

Fig. 15. Experimental and simulated discharge capacity as a function of discharge rate for cells with three different initial salt concentrations ($c^0 = 0.25$, 0.5, and 1.25 M). The solid symbols are experimental data and open symbols are model predictions with contact resistance and rate-dependent salt diffusion coefficient as adjustable parameters.

ing of real cells. Values of the salt diffusion coefficient in the solution phase between 3.35×10^{-6} and 1.7×10^{-6} cm^2/s provided the best fits to the experimental data over the range of rates. By allowing the solid-phase diffusion coefficient in the positive electrode to vary from 1×10^{-9} to 1×10^{-10} cm^2/s, an adequate fit to the data can also be achieved. Diffusion limitations are more prominent for thick cells than for medium and thin cells. Rate-dependent salt diffusion coefficients are probably an artifact of tortuous and inhomogeneous paths for salt diffusion inside the electrode/gelled polymer regions and reflect the inadequacy of the present simplified treatment of salt transport based on a binary electrolyte. During high-rate discharges, the solution-phase limitations are the major limiting factor.

7. List of symbols

a specific surface area [cm^{-1}]
A anode
c_s concentration of lithium in the solid [mol/dm^3]
c concentration of salt [mol/dm^3]
C theoretical capacity [mA h/g]; cathode
D salt diffusion coefficient [cm^2/s]
D_s diffusion coefficient of lithium in the solid electrode particles [cm^2/s]
i_o exchange current density for the insertion process [mA/cm^2]
m constant or mass [g]
p Bruggeman porosity parameter
R_c contact resistance [Ω cm^2]
R_s radius of electrode particles [μm]
S separator
t_+^0 lithium ion transference number
T temperature [°C]
x stoichiometric coefficient of negative electrode [Li$_x$C$_6$]
y stoichiometric coefficient of positive electrode [Li$_y$Mn$_2$O$_4$]

Greek

γ mass ratio of active material, positive to negative
δ_i thickness of cell component i [μm]
ε_i volume fraction of component i
κ ionic conductivity of electrolyte [S/cm]
σ electronic conductivity of solid matrix [S/cm]
ρ density of material [g/cm^3]

Subscripts

$+$ positive electrode
$-$ negative electrode
a   anode
c   cathode
cc   current collector
f   conductive filler
liq   liquid phase of plasticized electrolyte
p   polymer phase of plasticized electrolyte
s   separator
t   maximum concentration in intercalation material

Superscripts

0   with respect to the solvent or initial condition

References

[1] T.F. Fuller, M. Doyle, J. Newman, J. Electrochem. Soc. 141 (1994) 1.
[2] T.F. Fuller, M. Doyle, J. Newman, J. Electrochem. Soc. 141 (1994) 982.
[3] M. Doyle, J. Newman, A.S. Gozdz, C.N. Schmutz, J.-M. Tarascon, J. Electrochem. Soc. 143 (1996) 1890.
[4] C.N. Schmutz, J.-M. Tarascon, A.S. Gozdz, P.C. Warren, F.K. Shokoohi, Abstract 109, in: The Electrochemical Society Extended Abstract, Miami Beach, FL, Oct. 9–14, 1994 Vol. 94-21994, p. 172.
[5] M. Doyle, A.S. Gozdz, J. Newman, Joint general battery session, in: Electrochemical Society Meeting, Los Angeles, CA, May 8, 1996, 1996.
[6] A.S. Gozdz, J.-M. Tarascon, O.S. Gebizlioglu, C. Schmutz, P.C. Warren, F.K. Shokoohi, Abstract 117, in: The Electrochemical Society Extended Abstract, Miami Beach, FL, Oct. 9–14, 1994 Vol. 94-21994, p. 184.
[7] J.-M. Tarascon, A.S. Gozdz, C. Schmutz, F.K. Shokoohi, P.C. Warren, Solid State Ionics 86–88 (1996) 49.
[8] F.K. Shokoohi, P.C. Warren, S.J. Greaney, J.-M. Tarascon, A.S. Gozdz, G.G. Amatucci, in: 37th Proc. Power Sources Conf., 1996, p. 243.
[9] H. Dai, T.A. Zawodzinski, J. Electroanal. Chem. 459 (1998) 111.
[10] L. Christie, A.M. Chrische, C.A. Vincent, Electrochem. Solid State Lett. 2 (1999) 187.
[11] R. Pollard, J. Newman, J. Electrochem. Soc. 128 (1981) 491.
[12] H.S. Harned, B.B. Owen, The Physical Chemistry of Electrolytic Solutions, 3rd edn., Reinhold, New York, 1958.